

Lawrence Berkeley National Laboratory

Recent Work

Title

Discovery of Giant, Non-saturating Thermopower in Topological Semimetal at Quantum Limit

Permalink

<https://escholarship.org/uc/item/04t8576r>

Authors

Han, Fei
Andrejevic, Nina
Nguyen, Thanh
et al.

Publication Date

2019-11-13

Peer reviewed

Discovery of Giant, Non-saturating Thermopower in Topological Semimetal at Quantum Limit

Fei Han^{1*†}, Nina Andrejevic^{2†}, Thanh Nguyen^{1†}, Vladyslav Kozii^{3†}, Quynh Nguyen^{1,3}, Zhiwei Ding², Ricardo Pablo-Pedro¹, Shreya Parjan⁴, Brian Skinner³, Ahmet Alatas⁵, Ercan Alp⁵, Songxue Chi⁶, Jaime Fernandez-Baca⁶, Shengxi Huang⁷, Liang Fu^{3*}, Mingda Li^{1*}

¹Department of Nuclear Science and Engineering, Massachusetts Institute of Technology, Cambridge, MA 02139, USA

²Department of Materials Science and Engineering, Massachusetts Institute of Technology, Cambridge, MA 02139, USA

³Department of Physics, Massachusetts Institute of Technology, Cambridge, MA 02139, USA

⁴Department of Physics, Wellesley College, 106 Central St, Wellesley, MA 02481, USA

⁵Advanced Photon Source, Argonne National Laboratory, Lemont, IL 60439, USA

⁶Neutron Scattering Division, Oak Ridge National Laboratory, Oak Ridge, TN, 37831, USA

⁷Department of Electrical Engineering and Computer Science, The Pennsylvania State University, State College, PA 16801, USA

Thermoelectrics are promising by directly generating electricity from waste heat. However, (sub-) room-temperature thermoelectrics have been a long-standing challenge, due to the vanishing electronic entropy at low temperature¹. Topological materials²⁻⁴ offer a new avenue for energy harvesting applications⁵. Recent theories predicted that topological semimetals at the quantum limit can lead to non-saturating longitudinal thermopower⁶ as well as a quantized thermoelectric Hall conductivity approaching a universal value⁷. Here, we experimentally demonstrate the non-saturating thermopower and the signature of quantized thermoelectric Hall conductivity in topological Weyl semimetal (WSM) tantalum phosphide

[†]These authors contribute equally to this work.

*Corresponding authors: hanfei@mit.edu; liangfu@mit.edu; mingda@mit.edu.

(TaP). An ultrahigh longitudinal thermopower $S_{xx} = 1.1 \times 10^3 \mu\text{V/K}$ and a power factor $\sim 500 \mu\text{W/cm/K}^2$ are observed $\sim 40\text{K}$. Moreover, the thermoelectric Hall conductivity develops a plateau at high fields and low temperatures, which further collapses onto a single curve determined by universal constants. Our work highlights the unique WSM electronic structure and topological protection of Weyl nodes toward low-temperature energy harvesting applications.

Over two-thirds of global energy production is rejected as waste heat. Thermoelectrics are attractive by directly converting waste heat into electricity without moving parts. The efficiency of thermoelectric energy conversion is an increasing function of a dimensionless quantity $zT = \frac{\sigma S^2}{\kappa} T$, where σ , S , κ denote the electrical conductivity, thermopower, and total thermal conductivity, respectively. Conventional thermoelectrics largely focus on tuning the thermal and electrical conductivities. Many efforts, such as lowering dimensionality⁸, microstructuring^{9,10} and nanostructuring^{11,12}, share the same principle: By increasing the scattering of major heat carriers of long mean-free-path phonons without affecting the short mean-free-path electrons, a level of independent tunability between electrical conductivity σ and thermal conductivity κ can be achieved, such as the phonon-glass electron-crystal state¹³. However, less attention was paid to improve the thermopower S , even though the S^2 dependence of zT makes such improvement appealing. Moreover, thermopower S is proportional to the entropy per carrier and is therefore suppressed at reduced temperature¹⁴. For this reason, current thermoelectrics are generally effective only at elevated temperatures, and there is a pressing need for thermoelectrics that work efficiently at room-temperature and below. Filling this need requires new materials that can exhibit large electronic entropy at low temperatures while maintaining significant electrical conductivity.

One approach to creating large electronic entropy is to use bandstructure engineering through low carrier density, partially-filled carrier pockets¹⁵; a similar principle has also been applied to semimetals, such as WSMs, to explore arbitrarily low carrier densities¹⁶⁻¹⁸. However, there is a fundamental upper bound, set by the maximum entropy of the ideal classical gas. In this light, a magnetic field offers an additional incentive to break the upper bound, since the linear field-dependence of the density of states (DOS) enables accommodation of unbounded macroscopic number of states in each Landau level (LL), yet in conventional thermoelectrics, charge carriers will be localized at high B -field due to the cyclotron motion.

The recent development of topological WSMs brings new hope to break the fundamental limit met by conventional thermoelectrics, originating from the topological protection of electronic states. In particular, it is worthy to note that the WSM system has a unique $n=0$ LL. The $n=0$ LL in a WSM has a highly unusual *energy-independent* DOS $g(n=0) = N_f B e / 4\pi^4 \hbar^2 v_F$ increasing linearly with B , which can create huge electronic entropy. Meanwhile, it will remain gapless under high field thanks to the topological robustness of Weyl nodes. Consequently, recent theories predicted a non-saturating longitudinal thermopower and quantized thermoelectric Hall conductivity^{6,7}, where electrons and holes contribute additively to high thermoelectric performance without experiencing localization.

In this work, we carry out high-precision thermoelectric measurements using a centimeter-sized crystal WSM TaP (Figure 1a and b, and Methods). The Fermi level is fine-tuned through the synthesis procedure to approach the $n=0$ LL near the W2 Weyl node (Figure 1g). In this system, large, non-saturating longitudinal thermopower S_{xx} is observed, which exhibits linear dependence with B -field, and reaches 1100 $\mu\text{V/K}$ without saturation at $B=9\text{T}$. Additionally, the signature of the quantized thermoelectric Hall conductivity is observed, where at low-temperature and high fields, the

thermoelectric Hall conductivity $\alpha_{xy} \equiv [\mathbf{S}/\boldsymbol{\rho}]_{xy}$ is independent of B -field, and collapses into a single curve determined by number of fermion flavors, Fermi velocity, and universal constants. Moreover, evidence of Wiedemann-Franz law violation further indicates a breakdown of quasiparticle behaviors. Our work paves the way for a new class of materials that satisfies key criteria to fill the technological gap for low-temperature thermoelectric energy harvesting.

Quantum oscillations. We first present the longitudinal magnetoresistance (MR) data, where the magnetic field is applied perpendicular to current. Giant magnetoresistance was observed, where at $T < 25\text{K}$, the magnetoresistance $MR \equiv (R(9\text{T}) - R(0\text{T}))/R(0\text{T})$ exceeds $10^5\%$ (Figure 1c). This is a signature of electron-hole compensation, which is further confirmed by the two-band model fitting of conductivity, with $n_e = 2.39 \times 10^{19}/\text{cm}^3$ and $n_h = 2.35 \times 10^{19}/\text{cm}^3$ at $T = 2.5\text{K}$, along with a high mobility of $\sim 1 \times 10^5 \text{cm}^2/(\text{V} \cdot \text{s})$ (Supplementary Information III). The background-subtracted MR , termed ΔMR , exhibits Shubnikov-de Haas (SdH) oscillations, which are plotted against $1/B$ to determine the LL indices (Figure 1d). The LL fan diagram analysis indicates a contribution from two LLs: an $n=2$ LL and $n=0$ LL (Figure 1f). After Fourier transforming ΔMR , two low-frequency quantum oscillations $F_\alpha = 4\text{T}$ and $F_\beta = 18\text{T}$ are observed, matching the oscillation frequency from the carrier pockets at $n=0$ LL and $n=2$ LL. The intersection of the linear LL index plot (-0.037 for $n=0$ LL and $+0.065$ for $n=2$) lying between $-1/8$ to $+1/8$ indicates that the two pockets are both topologically nontrivial^{19,20} (Supplementary Information IV), from which we attribute the $n=2$ LL to the electron pocket of the W1 Weyl node, and the $n=0$ LL to the hole pocket of the W2 Weyl node (Figure 1g). Moreover, we see that the pocket the W2 Weyl node enters the quantum limit at $B \sim 3.8\text{T}$. There is an alternate way to see this without using the LL index intersection. For F_β , since the dispersion of Weyl fermions of the n^{th} LL at $k_z = 0$ is given by $E_n = \text{sgn}(n)v_F\sqrt{2e\hbar B|n|}$ while the

frequency F is related to the Fermi-surface area S_F as $F = \frac{\hbar}{2\pi e} S_F = \frac{E_F^2}{2e\hbar v_F^2}$, when $E_n \sim E_F$, we have $F \sim B|n|$. This leads to an agreement between $n=2$ LL and the measured $F_\beta = 18\text{T}$ at $B \sim 9\text{T}$. For F_α , the very low frequency 4T strongly suggests an extremely small Fermi surface. Since the spacing between $n=1$ and $n=0$ LLs is given by $E_1 - E_0 = v_F \sqrt{2e\hbar B} = E_F \sqrt{B/F}$, the condition to reach the quantum limit ($n=0$ LL) at the W2 Weyl node is met as long as $B > F_\alpha = 4\text{T}$. This value agrees well with the above LL index analysis.

Non-saturating thermopower. Having determined the carrier characteristics, we carried out thermoelectric measurements using a diagonal offset geometry (Figure 2a), where the electrical and thermal transport along both the longitudinal and transverse directions can be acquired together by flipping the field polarity (Supplementary Information V). The longitudinal thermopower S_{xx} is shown in Figure 2b, where a giant magnitude $S_{xx} = 1.07 \times 10^3 \mu\text{V/K}$ without sign of saturation is observed at $B = 9\text{T}$ and $T = 40\text{K}$. One prominent feature is that S_{xx} develops a double-peak behavior, which may be attributed to the two types of Weyl nodes – the higher mobility and lower density W2 node experiences reduced phonon scattering and thus can persist to higher temperatures. Quantitatively, it has been predicted that S_{xx} obeys a simple formula⁶:

$$S_{xx} = \frac{k_B^2}{\hbar^2} \frac{N_f}{12} \frac{TB}{v_F^{\text{eff}} (n_h - n_e)} \quad (1)$$

where N_f is number of Weyl nodes, $n_h - n_e$ is the net carrier density, and v_F^{eff} is an effective Fermi velocity that accounts for the presence of two types Weyl nodes in TaP, while the theory was originally derived for one type.

The linearity of S_{xx} with T and B is shown in Figures 2c and 2d, respectively. In particular, $S_{xx} \propto B$ is observed. It is also noteworthy that Eq. (1) is in quantitative agreement with our result if we adopt the fitted value of the v_F^{eff} using Eq. (3), discussed

shortly. Such quantitative agreement is valid across all fields and up to $\sim 40\text{K}$ and is a measure of the success of the effective model (Figure 2e). Moreover, a giant longitudinal power factor up to $PF \equiv S_{xx}^2/\rho_{xx} \sim 525 \mu\text{W}/\text{cm}/\text{K}^2$ is further achieved (Figure 2f). This is an order-of-magnitude higher than the peak values of conventional thermoelectrics (e.g., $PF(\text{SnSe}) \sim 10 \mu\text{W}/\text{cm}/\text{K}^2$)²¹.

Quantized thermoelectric Hall effect. Regarding the transverse thermoelectric properties, we see that the transverse thermopower S_{xy} also reaches a $\sim 10^3 \mu\text{V}/\text{K}$ peak value at $T = 40\text{K}$ (Figure 3a), moreover exhibiting a plateau. This plateau behavior is consistent with a recent report attributing it to the constant k -space volume regardless of the field-tuned Weyl-cone separation¹⁶, and should not be confused with the universal thermoelectric Hall conductivity α_{xy} . $\alpha_{xy} \equiv (S_{xy}\rho_{xx} + S_{xx}\rho_{xy})/(\rho_{xx}^2 + \rho_{xy}^2)$ is shown in Figure 3b, where in the low-temperature range, the flatness with respect to B -field starts to emerge. In particular, under the low-temperature $k_B T \ll E_F$ and high-field $B \gg E_F^2/\hbar e v_F^2$ limit, α_{xy} is predicted to approach the following universal value that is independent of B -field, disorder, carrier type or carrier density⁷:

$$\alpha_{xy,\text{ideal}} = \frac{\pi^2}{3} \frac{e k_B^2}{(2\pi\hbar)^2} \frac{N_f}{v_F^{\text{eff}}} T \quad (2)$$

The temperature dependence of α_{xy} is shown in Figure 3c, where we see that the linearity holds up to $T \sim 10\text{K}$. As a direct consequence, the α_{xy}/T curve collapses into a single curve at high fields (Figure 3d), where an ideal value $\alpha_{xy,\text{ideal}}/T = 0.6 \text{ A}/(\text{K}^2\text{m})$ is determined (Figure 3e) by using $v_F^{\text{eff}} = 1.2 \times 10^4 \text{ m/s}$ obtained from fitting with Eq. (3):

$$\alpha_{xy} = \frac{e N_f}{2\pi\hbar} \sum_{n=0}^{\infty} \int_0^{\infty} \frac{dk_z}{\pi} \left[s \left(\frac{\varepsilon_n^0(k_z) - \mu}{k_B T} \right) + s \left(\frac{\varepsilon_n^0(k_z) + \mu}{k_B T} \right) \right] \quad (3)$$

in which s is the electronic entropy function. The fitted chemical potential μ is consistent with the electrical transport measurements, while the Fermi velocity v_F^{eff} is lower than the v_F at W2, since the $n=2$ LL at W1 Weyl node has nonlinear dispersion and will reduce the v_F^{eff} , which is reasonable (Figure 3f, 3g and Supplementary Information VI and VII). As a result, the experimental values generally agree with the ideal value $\alpha_{xy,\text{ideal}}/T$, and the factor of 2 quantitative difference can be traced back to the electron pocket at W1 Weyl node yet to reach the quantum limit.

Breakdown of the Wiedemann-Franz Law. Wiedemann-Franz (WF) law is a robust empirical law stating that the ratio between the electronic thermal conductivity κ^e and electrical conductivity σ is related by a universal factor of Lorenz number:

$$L_0 \equiv \frac{\kappa^e}{\sigma T} = \frac{\pi^2}{3} \left(\frac{k_B}{e} \right)^2 = 2.44 \times 10^{-8} \text{ W}\Omega/\text{K}^2. \quad (4)$$

Recently, it has been reported that there is strong violation of WF law in 2D Dirac fluid of graphene²² and Weyl semimetal WP₂²³ due to the collective electron hydrodynamics. Other behaviors of electrons, like quantum criticality²⁴ or quasiparticle breakdown^{25,26}, can also lead to the WF law violation. In this light, it is worthwhile to examine the validity of the WF law in the field-induced high-entropy state of TaP. To do so, it is crucial to properly separate κ^e from the lattice thermal conductivity κ^{ph} . We adopt the following empirical relation by using the field-dependence of κ^e ²⁷:

$$\kappa_{xx}(T, B) = \kappa_{xx}^{ph}(T) + \frac{\kappa_{xx}^e(T)}{1 + \beta_e(T)B^m}. \quad (5)$$

where $\beta_e(T)$ is a measure of zero-field electron mean free path and m is a factor related to the nature of scattering. Figure 4a demonstrates an example for such separation procedure. Using this method, we see that the extracted lattice thermal conductivity κ^{ph} agrees well with the computed value from *ab initio* calculations (Figure 4b and

Methods), from which the phonon dispersions are also computed, and agree well with measured dispersion from inelastic scattering (Figure 4c). All these agreements indicate the reliability of the separation process. The corresponding electronic thermal conductivity κ^e and the Lorenz number is shown in Figure 4d and Figure 4e, respectively. At $B=0\text{T}$, the agreement with the WF law is good. However, as field increases to $B=9\text{T}$, a four-fold violation of WF law is observed (Figure 4d). The observed strong violation of the WF law hints at the possibility of field-driven quasiparticle breakdown in a large entropic system, and is subject to further investigation.

In this work, we demonstrated a giant, non-saturating longitudinal thermopower and a quantized thermoelectric Hall conductivity in a WSM, both showing quantitative agreement with recent theoretical proposals. In fact, these two features are linked: as the quantum limit is approached, $S_{xx} \sim \rho_{xy} \alpha_{xy}$, and thus a constant α_{xy} naturally indicates an $S_{xx} \propto B$ behavior since $\rho_{xy} \propto B$ at high field. In addition, a field-driven breakdown of the WF law is observed. Given the promising magnitudes of thermopower and power factor, our work sheds light on a few essential requirements that high-performance room-temperature thermoelectrics should meet. These include a way to create giant electronic entropy and reduce carrier density, and a way of evading localization while maintaining high electrical conductivity. Interestingly, the $n=0$ LL state with topologically protected Weyl node in a WSM satisfies all these requirements. Our work thus enables promising application of topological materials to lead the breakthrough of thermoelectric materials working below room temperature.

Note Added: When we were finalizing this manuscript, we became aware of a similar work on Dirac semimetal²⁸. The related work and our work mutually strengthened each other on the part of the quantized thermoelectric Hall effect.

Acknowledgements

The authors thank S.Y. Xu for the helpful discussions. N.A. acknowledges the support of the National Science Foundation Graduate Research Fellowship Program under Grant No. 1122374. T.N. thanks the support from the MIT SMA-2 Fellowship Program. V.K., B.S. and L.F. thank support from DOE Office of Basic Energy Sciences, Division of Materials Sciences and Engineering under Award DE-SC0018945. Q.N. thanks the support from MIT NSE UROP Program. Z. Ding thanks support from DOD Defense Advanced Research Projects Agency (DARPA) Materials for Transduction (MATRIX) program under Grant HR0011-16-2-0041. R.P.P. thanks the support from FEMSA and ITESM. B.S. is supported by the NSF STC “Center for Integrated Quantum Materials” under Cooperative Agreement No. DMR-1231319. L.F. is partly supported by the David and Lucile Packard Foundation. This research on neutron scattering used resources at the High Flux Isotope Reactor, a DOE Office of Science User Facility operated by the Oak Ridge National Laboratory. This research used resources of the Advanced Photon Source, a U.S. Department of Energy (DOE) Office of Science User Facility operated for the DOE Office of Science by Argonne National Laboratory under Contract No. DE-AC02-06CH11357.

Author contribution

M.L. and F.H. designed the experiments. V.K., B.S. and L.F. formulated the theory. F.H. synthesized the samples and perform the transport measurements, with the help of T.N., Q.N and S.P. N.A, T.N. and F.H. analyzed the data, with contribution from all the authors. Z.D. carried out *ab initio* calculations. N.A., T.N., F.H., R.P.P., M.L along with

A.A. E.A., S.C., J. F.-B. and S. H. performed inelastic scattering measurements. M.L. wrote the paper with input from all authors.

References

- 1 Rowe, D. M. *CRC handbook of thermoelectrics*. (CRC Press, 1995).
- 2 Hasan, M. Z. & Kane, C. L. Colloquium: Topological insulators. *Rev Mod Phys* **82**, 3045-3067, doi:10.1103/RevModPhys.82.3045 (2010).
- 3 Qi, X.-L. & Zhang, S.-C. Topological insulators and superconductors. *Rev Mod Phys* **83**, 1057-1110, doi:10.1103/RevModPhys.83.1057 (2011).
- 4 Armitage, N. P., Mele, E. J. & Vishwanath, A. Weyl and Dirac semimetals in three-dimensional solids. *Rev Mod Phys* **90**, 015001, doi:10.1103/RevModPhys.90.015001 (2018).
- 5 Heremans, J. P., Cava, R. J. & Samarth, N. Tetradymites as thermoelectrics and topological insulators. *Nature Reviews Materials* **2**, 17049, doi:10.1038/natrevmats.2017.49 (2017).
- 6 Skinner, B. & Fu, L. Large, nonsaturating thermopower in a quantizing magnetic field. *Science Advances* **4**, eaat2621, doi:ARTN eaat2621 10.1126/sciadv.aat2621 (2018).
- 7 Kozii, V., Skinner, B. & Fu, L. Thermoelectric Hall conductivity and figure of merit in Dirac/Weyl materials. *eprint arXiv:1902.10123*, arXiv:1902.10123 (2019).
- 8 Dresselhaus, M. S. *et al.* New Directions for Low-Dimensional Thermoelectric Materials. *Advanced Materials* **19**, 1043-1053, doi:10.1002/adma.200600527 (2007).
- 9 Biswas, K. *et al.* High-performance bulk thermoelectrics with all-scale hierarchical architectures. *Nature* **489**, 414-418, doi:10.1038/nature11439 (2012).
- 10 Il Kim, S. *et al.* Dense dislocation arrays embedded in grain boundaries for high-performance bulk thermoelectrics. *Science* **348**, 109-114 (2015).
- 11 Minnich, A. J., Dresselhaus, M. S., Ren, Z. F. & Chen, G. Bulk nanostructured thermoelectric materials: current research and future prospects. *Energy & Environmental Science* **2**, 466, doi:10.1039/b822664b (2009).
- 12 Vineis, C. J., Shakouri, A., Majumdar, A. & Kanatzidis, M. G. Nanostructured thermoelectrics: big efficiency gains from small features. *Adv Mater* **22**, 3970-3980, doi:10.1002/adma.201000839 (2010).
- 13 Snyder, G. J. & Toberer, E. S. Complex thermoelectric materials. *Nat Mater* **7**, 105, doi:10.1038/nmat2090 (2008).
- 14 Heremans, J. P. *et al.* Enhancement of Thermoelectric Efficiency in PbTe by Distortion of the Electronic Density of States. *Science* **321**, 554, doi:10.1126/science.1159725 (2008).
- 15 Pei, Y. *et al.* Convergence of electronic bands for high performance bulk thermoelectrics. *Nature* **473**, 66-69, doi:10.1038/nature09996 (2011).

- 16 Caglieris, F. *et al.* Anomalous Nernst effect and field-induced Lifshitz transition in the Weyl semimetals TaP and TaAs. *Physical Review B* **98**, doi:10.1103/PhysRevB.98.201107 (2018).
- 17 Watzman, S. J. *et al.* Dirac dispersion generates unusually large Nernst effect in Weyl semimetals. *Physical Review B* **97**, doi:10.1103/PhysRevB.97.161404 (2018).
- 18 Sharma, G., Moore, C., Saha, S. & Tewari, S. Nernst effect in Dirac and inversion-asymmetric Weyl semimetals. *Physical Review B* **96**, doi:10.1103/PhysRevB.96.195119 (2017).
- 19 Murakawa, H. *et al.* Detection of Berry's Phase in a Bulk Rashba Semiconductor. *Science* **342**, 1490, doi:10.1126/science.1242247 (2013).
- 20 Zhao, Y. *et al.* Anisotropic Fermi Surface and Quantum Limit Transport in High Mobility Three-Dimensional Dirac Semimetal Cd₃As₂. *Physical Review X* **5**, doi:10.1103/PhysRevX.5.031037 (2015).
- 21 Zhao, L. D. *et al.* Ultralow thermal conductivity and high thermoelectric figure of merit in SnSe crystals. *Nature* **508**, 373-377, doi:10.1038/nature13184 (2014).
- 22 Crossno, J. *et al.* Observation of the Dirac fluid and the breakdown of the Wiedemann-Franz law in graphene. *Science* **351**, 1058-1061, doi:10.1126/science.aad0343 (2016).
- 23 Gooth, J. *et al.* Thermal and electrical signatures of a hydrodynamic electron fluid in tungsten diphosphide. *Nature Communications* **9**, doi:ARTN 4093 10.1038/s41467-018-06688-y (2018).
- 24 Tanatar, M. A., Paglione, J., Petrovic, C. & Taillefer, L. Anisotropic violation of the Wiedemann-Franz law at a quantum critical point. *Science* **316**, 1320-1322, doi:10.1126/science.1140762 (2007).
- 25 Lee, S. *et al.* Anomalously low electronic thermal conductivity in metallic vanadium dioxide. *Science* **355**, 371, doi:10.1126/science.aag0410 (2017).
- 26 Hartnoll, S. A. Theory of universal incoherent metallic transport. *Nat Phys* **11**, 54-61, doi:10.1038/nphys3174 (2014).
- 27 Ocana, R. & Esquinazi, P. Thermal conductivity tensor in YBa₂Cu₃O_{7-x}: Effects of a planar magnetic field. *Physical Review B* **66**, doi:ARTN 064525 10.1103/PhysRevB.66.064525 (2002).
- 28 Zhang, W. *et al.* Quantized plateau in the thermoelectric Hall conductivity for Dirac electrons in the extreme quantum limit. *eprint arXiv:1904.02157*, arXiv:1904.02157 (2019).

Methods

High-quality Single-crystal Growth. The single crystals of TaP were prepared by the vapor transport method. 3 grams of Ta (Beantown Chemical, 99.95%) and P (Beantown Chemical, 99.999%) powders were weighted, mixed and ground in a glovebox. The mixed powders were flame-sealed in a quartz tube which was subsequently heated to 700°C and dwelled for 20 hours for a pre-reaction. The obtained TaP powders were sealed in another quartz tube with 0.4 gram of I₂ (Sigma Aldrich, >=99.8%) added. The tube containing TaP and I₂ was then horizontally placed in a two-zone furnace. To improve the crystal size and quality, instead of setting a 100°C temperature difference, we gradually increased the temperature difference from zero until the I₂ transport agent started to flow. This process seems to be furnace- and distance- specific. In our case, the optimal temperatures for the two zones are 900°C and 950°C, respectively, and the distance between the two heating zone is constantly optimized. With the help of the transport agent I₂, the TaP source materials transferred from the cold end of the tube to the hot end and condensed at the hot end in a single-crystalline form in 14 days. The resulting products of TaP single crystals are centimeter-sized and have a metallic luster. Figure S1 exhibits a typical sample of TaP crystals.

Sample Preparation for Measurements. Due to the very high electrical and thermal conductivities of TaP, it is difficult to do high-precision electrical and thermal transport measurements on the as-grown crystals. To magnify the electrical resistance and the temperature gradient in the electrical and thermal transport measurements, one piece of crystal was polished down to thin along the *c*-axis. Figure S2 shows top and side views of a thinned-down crystal whose thickness is only 0.17 mm.

Electrical and Thermal Transport Measurements. The electrical and thermal transport measurements were carried out with the electrical transport option (ETO) and the thermal transport option (TTO) of PPMS, respectively. The data about the quantum oscillations was measured with the ETO whereas the data about the thermoelectric (including resistivity) with the TTO. When we performed the ETO measurements we adopted a standard six-probe configuration and connected the longitudinal and transverse probes to two independent measurement channels. The details about the ETO measurement can be found in Figure S3a and Supplementary Information III. However, because the TTO has only one measurement channel, to measure the longitudinal and transverse thermal conductivities (κ_{xx} and κ_{xy}), resistivities (ρ_{xx} and ρ_{xy}) and Seebeck coefficients (S_{xx} and S_{xy}) simultaneously, we used a diagonal offset probe geometry for the thermal transport measurement, as shown in Figure S4a and S5a. For the detailed description about the TTO measurement, please check Supplementary Information IV.

Computational Details. All the *ab initio* calculations are performed by Vienna Ab Initio Package (VASP)^{M1,M2} with projector-augmented-wave (PAW) pseudopotentials and Perdew-Burke-Ernzerhof (PBE) for exchange-correlation energy functional^{M3}. The geometry optimization of the conventional cell was performed with a $6 \times 6 \times 2$ Monkhorst-Pack grid of k-point sampling. The second-order and third-order force constants was calculated using a real space supercell approach with a $3 \times 3 \times 1$ supercell. The Phonopy package^{M4} was used to obtain the second-order force constants. The thirdorder.py and ShengBTE packages^{M5} were used to obtain the third-order force constants and relaxing time approximation was used to calculate the thermal conductivity. A cutoff radius of about 0.42 nm was used, which corresponds to including the fifth nearest neighbor when determining the third-order force constants.

To get the equilibrium distribution function and scattering rates using the third-order force constants, the first Brillouin zone was sampled with $30 \times 30 \times 10$ mesh.

Inelastic Scattering. Inelastic neutron scattering measurements were performed on the HB1 triple-axis spectrometer at the High-Flux Isotope Reactor at the Oak Ridge National Laboratory. We used a fixed $E_f = 14.7$ meV with 48° – 40° – 40° – 120° collimation and Pyrolytic Graphite filters to eliminate higher-harmonic neutrons. Measurements were performed using closed-cycle refrigerators between room temperature and the base temperature 4 K. Inelastic X-ray scattering was performed on the high-energy resolution inelastic x-ray (HERIX) instrument at sector 3-ID beamline of the Advanced Photon Source, Argonne National Laboratory with incident beam energy of 21.657 keV ($\lambda=0.5725\text{\AA}$) and an overall energy resolution of 2.1 meV^{M6-M8}. Incident beam focused on the sample using toroidal and KB mirror system. FWHM of beam size at sample position was $20 \times 20 \mu\text{m}^2$ (V \times H). The spectrometer was functioning in the horizontal scattering geometry with a horizontally polarized radiation. The scattered beam was analyzed by a diced and spherically curved silicon (18 6 0) analyzers working at backscattering angle. The basic principles of such instrumentations are discussed elsewhere^{M9,M10}.

- M1 Kresse, G. & Furthmuller, J. Efficiency of ab-initio total energy calculations for metals and semiconductors using a plane-wave basis set. *Comp Mater Sci* **6**, 15-50, doi:Doi 10.1016/0927-0256(96)00008-0 (1996).
- M2 Kresse, G. & Joubert, D. From ultrasoft pseudopotentials to the projector augmented-wave method. *Physical Review B* **59**, 1758-1775, doi:DOI 10.1103/PhysRevB.59.1758 (1999).
- M3 Perdew, J. P., Burke, K. & Ernzerhof, M. Generalized gradient approximation made simple. *Phys Rev Lett* **77**, 3865-3868, doi:DOI 10.1103/PhysRevLett.77.3865 (1996).
- M4 Togo, A. & Tanaka, I. First principles phonon calculations in materials science. *Scripta Materialia* **108**, 1-5, doi:10.1016/j.scriptamat.2015.07.021 (2015).

- M5 Li, W., Carrete, J., Katcho, N. A. & Mingo, N. ShengBTE: A solver of the Boltzmann transport equation for phonons. *Comput Phys Commun* **185**, 1747-1758, doi:10.1016/j.cpc.2014.02.015 (2014).
- M6 Sinn, H. *et al.* An inelastic X-ray spectrometer with 2.2 meV energy resolution. *Nucl Instrum Meth A* **467**, 1545-1548, doi:Doi 10.1016/S0168-9002(01)00755-0 (2001).
- M7 Alatas, A. *et al.* Improved focusing capability for inelastic X-ray spectrometer at 3-ID of the APS: A combination of toroidal and Kirkpatrick-Baez (KB) mirrors. *Nucl Instrum Meth A* **649**, 166-168, doi:10.1016/j.nima.2010.11.068 (2011).
- M8 Toellner, T. S., Alatas, A. & Said, A. H. Six-reflection meV-monochromator for synchrotron radiation. *J Synchrotron Radiat* **18**, 605-611, doi:10.1107/S0909049511017535 (2011).
- M9 Sinn, H. Spectroscopy with meV energy resolution. *J Phys-Condens Mat* **13**, 7525-7537, doi:Doi 10.1088/0953-8984/13/34/305 (2001).
- M10 Burkel, E. Determination of phonon dispersion curves by means of inelastic x-ray scattering. *J Phys-Condens Mat* **13**, 7627-7644, doi:Doi 10.1088/0953-8984/13/34/310 (2001).

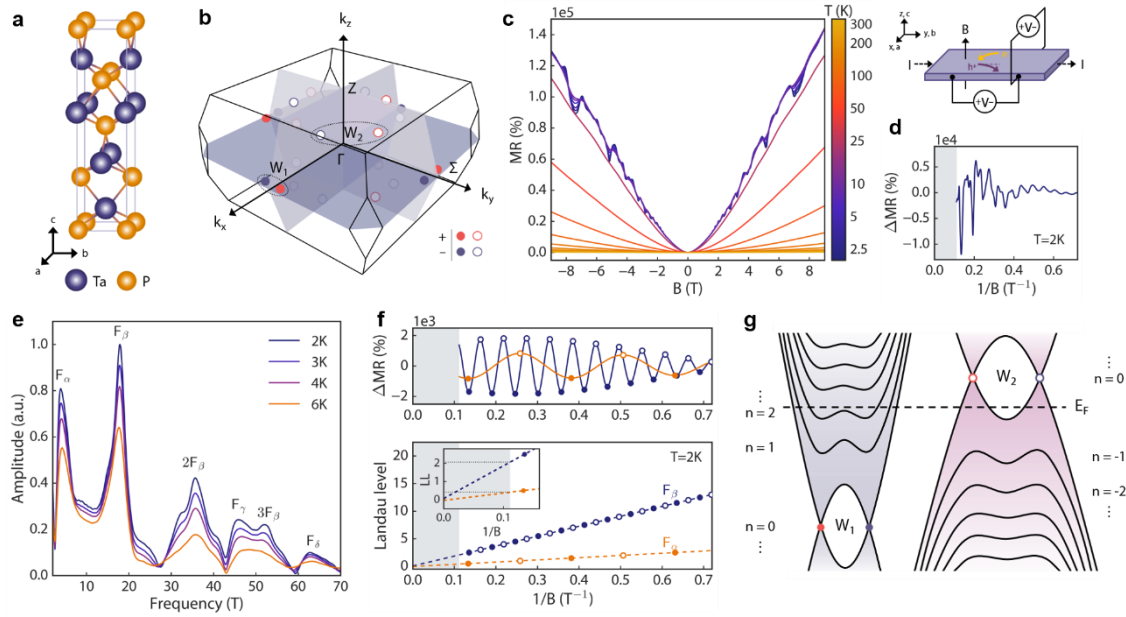


Figure 1. Quantum oscillation of TaP. (a) The inversion-symmetry-breaking crystal structure and (b) the Brillouin zone of TaP, highlighting the locations of the inequivalent Weyl nodes W_1 (filled circles) and W_2 (empty circles). The Weyl nodes are paired as source “+” and sink “-” of Berry curvature, separated in momentum space. (c) Magnetoresistance (MR) as a function of magnetic field at different temperatures from 2.5K to 300K. A high ($>10^5\%$) MR ratio is observed. (d) The MR measurement configuration (top) and relative ΔMR as a function of $1/B$ (bottom). (e) The Fourier transform of the MR showing a low oscillation frequency $F_\alpha=4T$. This is a signature that in addition to the electron pocket from W_1 Weyl node contributing to $F_\delta=18T$, we are very close to the W_2 Weyl node. (f) The SdH oscillation and Landau level index plot, from which we obtained an $n=2$ Landau level and another $n=0$ Landau level. (g) The schematic bandstructure at finite magnetic fields of our TaP sample.

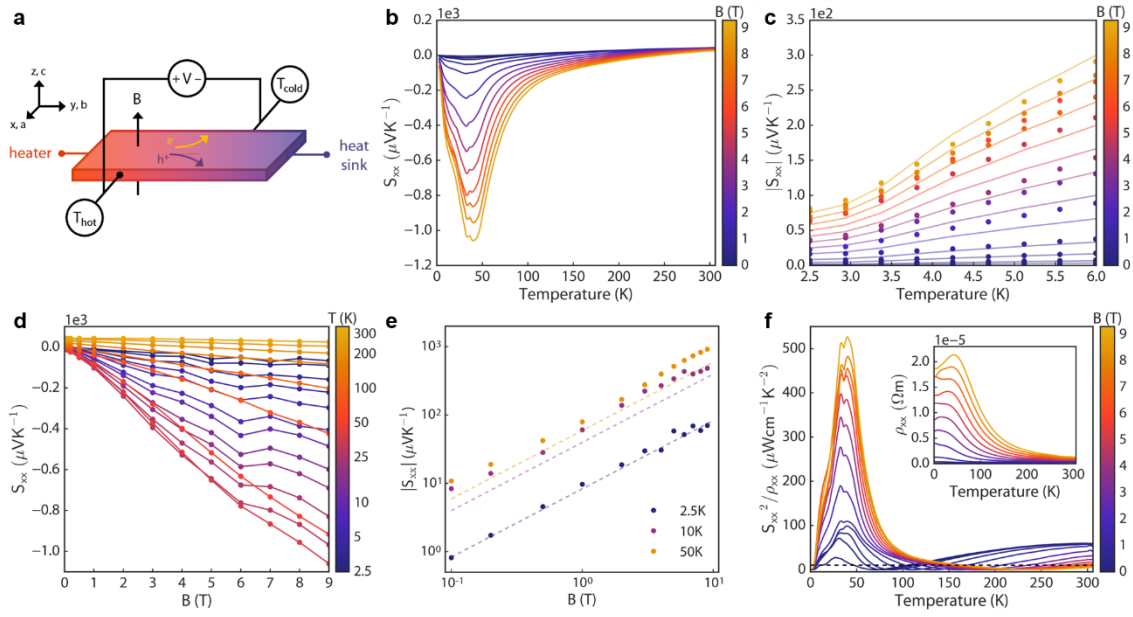


Figure 2. Non-saturating thermopower at high fields. (a) The schematics of the diagonal offset thermoelectric measurement geometry. (b) Longitudinal thermopower S_{xx} as a function of temperature at various fields. The double peaks emerge at $\sim 33\text{K}$ and $\sim 40\text{K}$. (c) S_{xx} at low-temperature range, showing the quasi-linearity growth as a function of temperature. (d) S_{xx} replotted as a function of B , showing the unbounded linear growth with field. The onset of the linear behavior indicates the entering into the quantum limit regime. The oscillatory behavior $\sim 20\text{K}$ at $B=6\text{T}$ is caused by the quantum oscillation effect. (e) S_{xx} as a function of B at a few representative temperatures. The dashed lines are prediction using Eq. (1) by substituting the fitted v_F from Eq. (3). (f) The power factor as a function of temperature. The black-dashed line is a reference peak value for SnSe.

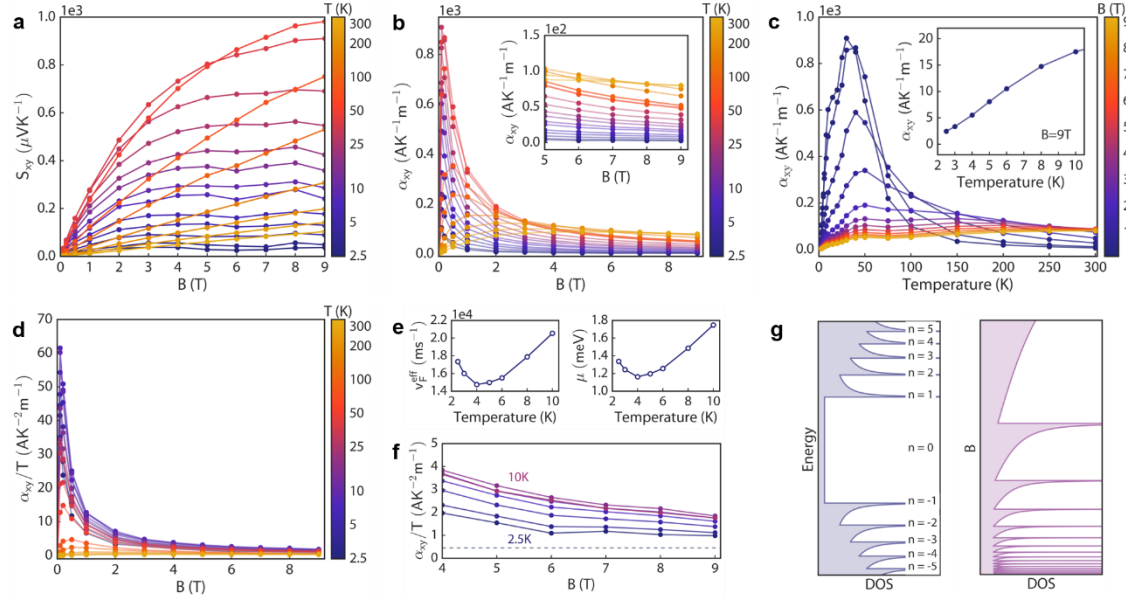


Figure 3. The Quantized thermoelectric Hall effect. (a) Transverse thermopower S_{xy} as a function of magnetic field at different temperatures. (b) Thermoelectric Hall conductivity α_{xy} as a function of magnetic field at different temperatures. The peak value is caused by the finite scattering effect. (c) Thermoelectric Hall conductivity α_{xy} as a function of temperature at various fields. The inset shows a linear behavior of the α_{xy} versus T curves at low temperatures. (d) α_{xy}/T as a function of magnetic field collapses to a constant plateau at the quantum limit. (e) Values of the bandstructure parameters obtained by fitting α_{xy} versus T using Eq. (3). (f) Enlarged view of α_{xy}/T at low temperatures indicating a convergence to the quantum limit. The gray dashed line gives the universal value obtained via fit of α_{xy}/T . (g) The DOS of each LL, highlighting the unique $n=0$ LL in a WSM. At high-enough B , $n=0$ LL drives the $\text{DOS} \propto B$.

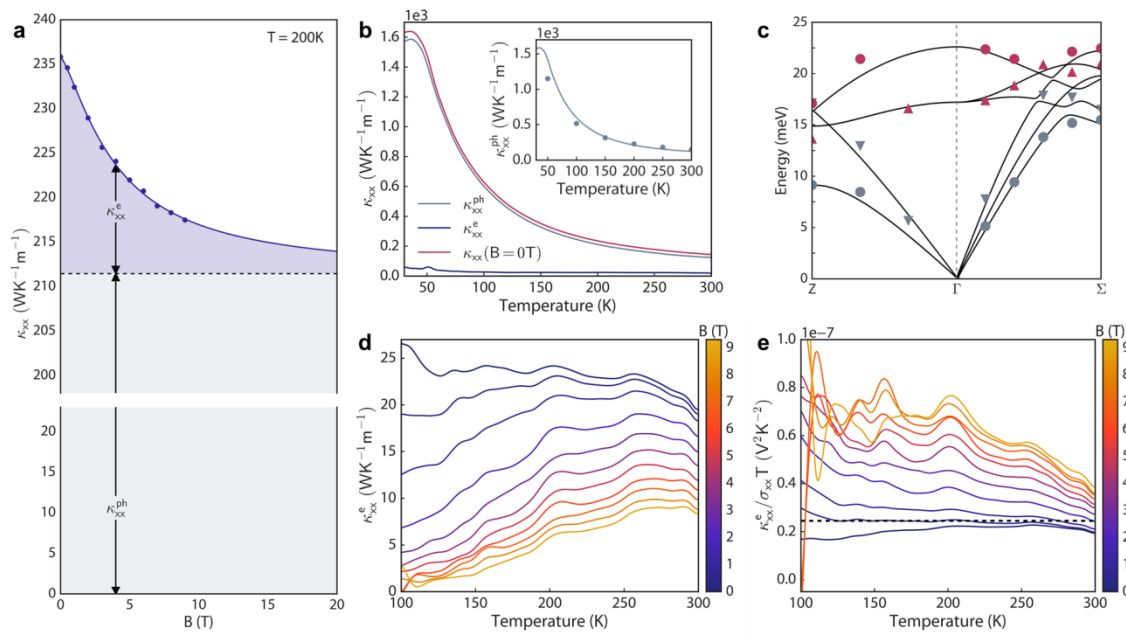


Figure 4. The Wiedemann-Franz Law. (a) The schematics of the separation process of electronic thermal conductivity κ_{xx}^e from the lattice thermal conductivity κ_{xx}^{ph} using the field-dependence. (b) Separation of phonon and electronic contributions to the longitudinal thermal conductivity with inset displaying a computation (scattered points) of the phonon thermal conductivity from first principles. (c) Experimentally measured values of phonon modes (scattered points) of TaP along high-symmetry line Z- Γ - Σ taken by inelastic x-ray and neutron scattering with accompanying *ab initio* calculation (solid lines), displaying good agreement between *ab initio* calculations and experiment. (d) The electronic contribution of the thermal conductivity as a function of temperature at various fields. (e) The Lorenz number as a function of temperature at various fields. The black line indicates the theoretical value of the Wiedemann-Franz law.

Discovery of Giant, Non-saturating Thermopower in Topological Semimetal at Quantum Limit: Supplementary Information

Fei Han^{1*†}, Nina Andrejevic^{2†}, Thanh Nguyen^{1†}, Vladyslav Kozii^{3†}, Quynh Nguyen^{1,3},
Zhiwei Ding², Ricardo Pablo-Pedro¹, Shreya Parjan⁴, Brian Skinner³, Ahmet Alatas⁵,
Ercan Alp⁵, Songxue Chi⁶, Jaime Fernandez-Baca⁶, Shengxi Huang⁷, Liang Fu^{3*},
Mingda Li^{1*}

¹Department of Nuclear Science and Engineering, Massachusetts Institute of Technology,
Cambridge, MA 02139, USA

²Department of Materials Science and Engineering, Massachusetts Institute of Technology,
Cambridge, MA 02139, USA

³Department of Physics, Massachusetts Institute of Technology, Cambridge, MA 02139, USA

⁴Department of Physics, Wellesley College, 106 Central St, Wellesley, MA 02481, USA

⁵Advanced Photon Source, Argonne National Laboratory, Lemont, IL 60439, USA

⁶Neutron Scattering Division, Oak Ridge National Laboratory, Oak Ridge, TN, 37831, USA

⁷Department of Electrical Engineering and Computer Science, The Pennsylvania State
University, State College, PA 16801, USA

[†]These authors contribute equally to this work.

*Corresponding authors: hanfei@mit.edu; liangfu@mit.edu; mingda@mit.edu.

Contents

- I. High-quality Single-crystal Growth
- II. Sample Preparation for Measurements
- III. Carrier Concentration and Mobility
- IV. Landau Level and Quantum Limit
- V. Data Analysis for Thermoelectric Measurement
- VI. Thermoelectric Hall Conductivity
- VII. Consistency of Charge Neutrality
- VIII. X-Ray and Neutron Scattering Measurement Details
- IX. Separation of Phonon and Electron Contributions to Thermal Conductivity

I. High-quality Single-crystal Growth

We successfully obtained centimeter-sized single crystals of TaP using the vapor transport method described in the “Methods” section of the main text. A typical crystal is shown in Figure S1.

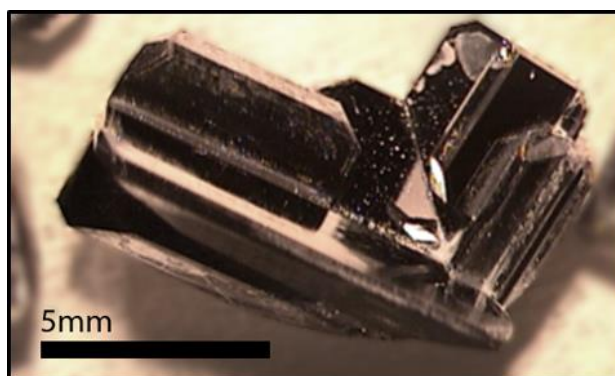


Figure S1. Single crystals of TaP grown by the vapor transport method.

II. Sample Preparation for Measurements

As introduced in the “Methods” section of the main text, to conduct high-precision measurement of electrical and thermal conductivity on TaP, we performed a thinning-down process on the crystals. Figure S2 displays the thinned-down crystal we used for the thermoelectric measurement. Its thickness is only 0.17mm.

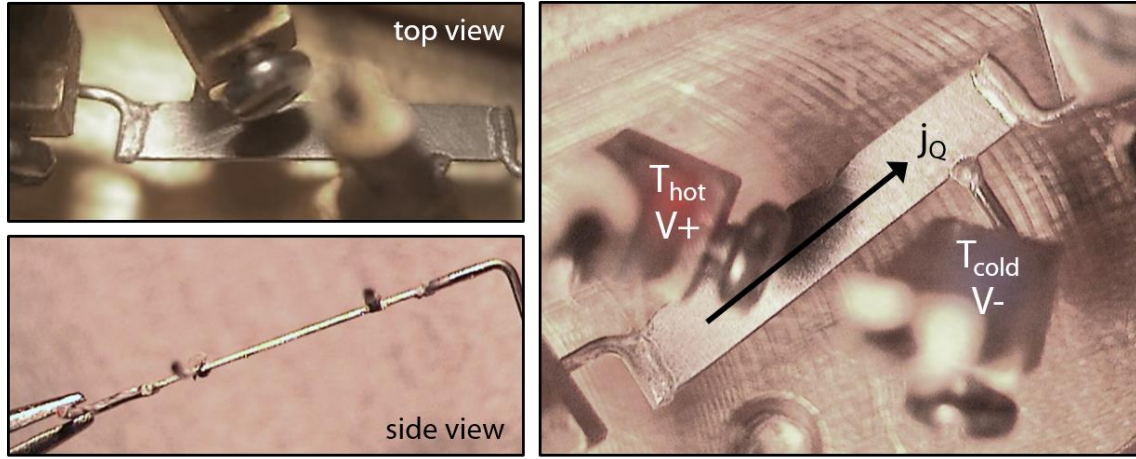


Figure S2. Top and side view of the thinned-down sample we used for the thermoelectric measurement.

III. Carrier Concentration and Mobility

To experimentally validate the prediction of a quantized thermoelectric Hall effect requires information about the carrier concentration and mobility. To extract this information, we carried out a delicate electrical transport measurement with the electrical transport option (ETO) of the physical property measurement system (PPMS). The measurement was done using a standard six-probe geometry, schematically shown in Figure S3a. With the symmetric probe configuration, the measured longitudinal resistivity ρ_{xx} is symmetric with respect to the applied magnetic field, while the transverse resistivity ρ_{xy} is antisymmetric, as shown in Figure S3b and c. In both ρ_{xx} and ρ_{xy} , strong Shubnikov-de Haas (SdH) oscillations can be observed at low temperatures. The oscillation is preserved up to 25K, indicating high quality crystallization in our

sample, as the temperature damping effect would otherwise eliminate the quantum oscillation at this relatively high temperature.

Because the contacts on the sample were made manually with silver epoxy, the measured data exhibit slight asymmetry due to slight misalignment of the contacts. To eliminate the effect of the contact misalignment, we averaged the ρ_{xx} and ρ_{xy} using the equations listed below:

$$\rho_{xx} = \frac{\rho_{xx}(+B) + \rho_{xx}(-B)}{2}, \quad \rho_{xy} = \frac{\rho_{xy}(+B) - \rho_{xy}(-B)}{2}. \quad (\text{S1})$$

Then we calculated the longitudinal and transverse conductivities σ_{xx} and σ_{xy} using the following equations:

$$\sigma_{xx} = \frac{\rho_{xx}}{\rho_{xx}^2 + \rho_{xy}^2}, \quad \sigma_{xy} = -\frac{\rho_{xy}}{\rho_{xx}^2 + \rho_{xy}^2}. \quad (\text{S2})$$

The field dependence of σ_{xx} and σ_{xy} at various temperatures is shown in Figure S3d and e. To extract the carrier concentration and mobility, we simultaneously fit the σ_{xx} and σ_{xy} data as functions of B using a two-band model defined by:

$$\sigma_{xx} = \frac{n_e \mu_e e}{1 + (\mu_e B)^2} + \frac{n_h \mu_h e}{1 + (\mu_h B)^2} \quad (\text{S3})$$

$$\sigma_{xy} = \left[n_h \mu_h^2 \frac{1}{1 + (\mu_h B)^2} - n_e \mu_e^2 \frac{1}{1 + (\mu_e B)^2} \right] eB,$$

where n_e and n_h denote the electron and hole carrier densities, μ_e and μ_h are the corresponding mobilities, and e is the elementary charge. We thereby extract the electron and hole carrier densities and mobilities as functions of temperature, as shown

in Figure S3f and g. The electron and hole concentrations are nearly compensated at low temperatures. This proves the origin of the giant magnetoresistance.

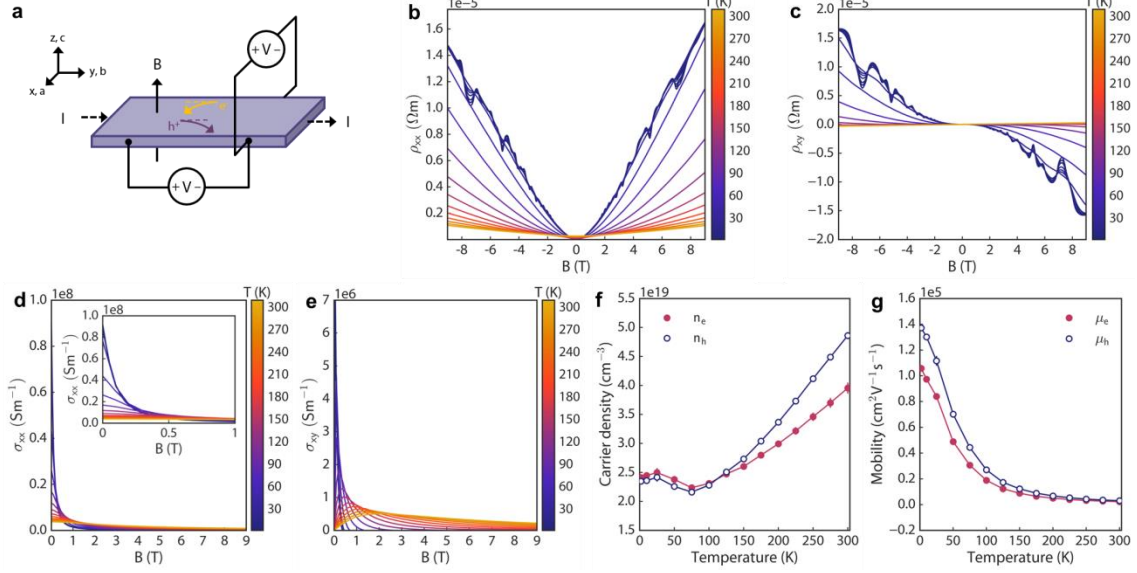


Figure S3. (a) Schematic diagram of the electrical transport measurement in the six-probe geometry. Longitudinal and transverse resistivities and conductivities (b) ρ_{xx} , (c) ρ_{xy} , (d) σ_{xx} and (e) σ_{xy} as functions of magnetic field at different temperatures. (f) Carrier concentration and (g) mobility of electrons and holes resulting from the two-band model fitting.

IV. Landau Level and Quantum Limit

The quantized thermoelectric Hall effect considered in this work is theoretically predicted to exist in the quantum limit of Dirac/Weyl semimetals^{S1,S2}. Therefore, to examine the validity of the theoretical prediction, we first verify that the quantum limit condition is satisfied by Weyl fermions in our TaP sample. To do this, we performed a thorough analysis of the quantum oscillations observed in the electrical transport measurement, as shown in Figure 1 in the main text. The quantum oscillation data shown in Figure 1d of the main text was obtained by subtracting a smooth background from the magnetoresistance (MR) data, Figure 1c, where ΔMR is defined according to:

$$\Delta MR = \frac{\rho_{xx}(B) - \rho_{xx}(B=0T)}{\rho_{xx}(B=0T)} \times 100\% . \quad (S4)$$

From the fast Fourier transform (FFT) analysis depicted in Figure 1e, we determine that the quantum oscillations in our sample are dominated by two oscillation frequencies: one at 4T and the other at 18T (named F_α and F_β , respectively). After performing a standard signal filtering process by taking the inverse FFT of a narrow window around the 4T and 18T frequencies individually, we isolate the two oscillation components from the pristine data and determine the corresponding Landau levels (LL) by assigning an integer (half-integer) value to the oscillation maxima (minima), as shown in Figure 1f. From the LL index fan, we conclude that in our TaP sample, the α Fermi pocket corresponding to the 4T frequency is in the $n=0$ LL at our maximum field of $B=9T$, whereas the β Fermi pocket corresponding to the 18T frequency is in the $n=2$ LL. Specifically, the α Fermi pocket enters the quantum limit (lowest LL) approximately at 3.8T, and the β Fermi pocket will reach the quantum limit at an approximate field of 16T. The linear fitting of the LL index as a function of $1/B$ yields intercepts of -0.037 and 0.065 for α and β , respectively. Both are in the range of -1/8 to 1/8, proving the bands in the α and β Fermi pockets are topologically non-trivial and thus Weyl cones are present^{S3}. From this, we can further conclude that the Weyl Fermions in the smallest Fermi pocket of TaP are well within the quantum limit at our maximum applied field, whereas the Weyl fermions in the second smallest Fermi pocket are nearing the onset of the quantum limit.

V. Data Analysis for Thermoelectric Measurement

Figure S4a schematically shows the principle behind the thermal transport measurement in the diagonal offset probe geometry. Using the thermal transport option (TTO) of the PPMS, the heater on the left end of the thinned-down crystal and heat sink on the right establish a continuous heat flow along the a or b axis (a and b are equivalent for this tetragonal system), as shown in Figure S2. The thermal conductivity is directly calculated by the PPMS using the applied heater power, the resulting temperature difference ΔT detected between the two thermometers, and the sample dimension. The voltage drop ΔV between the two thermometers is monitored simultaneously, which yields the Seebeck signals by calculation of $-\frac{\Delta V}{\Delta T}$. A magnetic field was applied along the c axis for detecting the proposed quantized thermoelectric Hall effect. Figure S4b shows the temperature dependence of thermal conductivity of TaP at 9T and -9T. From this plot, we note that the thermal conductivities at positive and negative magnetic fields have a very slight difference. This indicates that the thermoelectric Hall effect (the transverse movement of thermal electrons in the presence of a magnetic field) provides a negligible but observable heat flow along the transverse direction. To extract the longitudinal thermal conductivity from the measured thermal conductivity, we use the following equations:

$$\rho_{th,xx} = \frac{\kappa(+B) + \kappa(-B)}{2\kappa(+B)\kappa(-B)}, \quad \rho_{th,xy} = \frac{\kappa(+B) - \kappa(-B)}{2\kappa(+B)\kappa(-B)} \times \frac{L}{W}, \quad (S5)$$

and

$$\kappa_{xx} = \frac{\rho_{th,xx}}{\rho_{th,xx}^2 + \rho_{th,xy}^2}, \quad (S6)$$

where L and W represent the length-wise and the width-wise separation between the two thermometers. Figure S4c displays the obtained longitudinal thermal conductivity κ_{xx} as a function of temperature at different magnetic fields. From the inset of Figure S4c, we see that the applied magnetic field gradually suppresses the longitudinal thermal conductivity. This phenomenon is consistent with the giant magnetoresistance, as both originate from the greatly elevated electron scattering induced by the magnetic field. The magnitude of the thermal conductivity of TaP is very large compared to most materials, which explains the importance of thinning the sample prior to measurement. The Seebeck signals at 0T, 9T and -9T are plotted in Figure S4d, from which giant magnetic field-induced Seebeck signals can be observed at 9T and -9T. The data for 9T and -9T are asymmetrical due to the mutual presence of longitudinal and transverse Seebeck signals. We use the following equations to calculate the longitudinal and transverse Seebeck coefficients S_{xx} and S_{xy} :

$$S_{xx} = \frac{S_{\text{meas}}(+B) + S_{\text{meas}}(-B)}{2}, \quad S_{xy} = \frac{S_{\text{meas}}(+B) - S_{\text{meas}}(-B)}{2} \times \frac{L}{W}. \quad (\text{S7})$$

The temperature dependence of S_{xx} and S_{xy} collected at different magnetic fields is presented in Figure S4e and f. It is obvious that the applied magnetic fields induce giant Seebeck coefficients along both longitudinal and transverse directions. The longitudinal Seebeck coefficient S_{xx} does not appear to saturate with increasing field up to the highest measured field of 9T. By contrast, S_{xy} tends to saturate at high magnetic fields. Another novel behavior in S_{xx} and S_{xy} is the presence of a double-peak feature around $T=40\text{K}$. We provide a clear explanation of this feature in the main text.

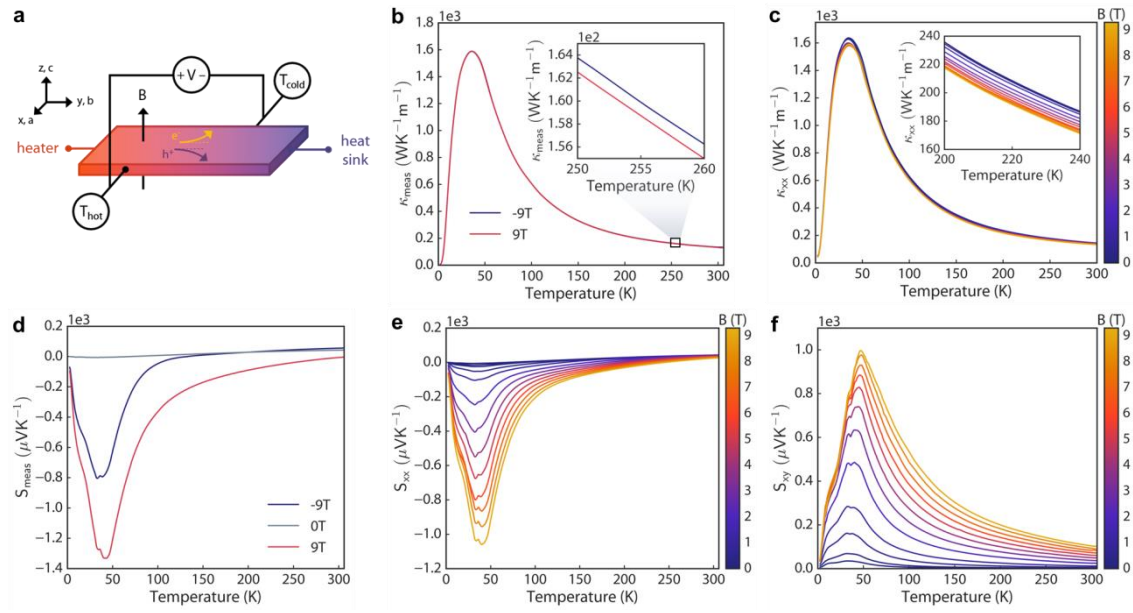


Figure S4. (a) Schematic diagram of the thermal transport measurement. (b) Thermal conductivities of TaP at 9T and -9T. (c) Longitudinal thermal conductivity of TaP as a function of temperature at various fields. (d) Measured Seebeck signals at 0T, 9T and -9T for the diagonal offset probe geometry. (e) Longitudinal and (f) transverse Seebeck coefficients S_{xx} and S_{xy} as functions of temperature at different magnetic fields.

After performing the thermal transport measurement at a certain temperature, a subsequent electrical transport measurement at the same temperature is made in the TTO. The inset of Figure S5a shows the schematic diagram for the electrical transport measurement in the diagonal offset geometry. In the presence of a magnetic field, the system applies an electrical current along the a or b axis, and the voltmeter between the diagonal offset probes detects the voltage drop which contains both longitudinal and transverse components. The longitudinal resistivity ρ_{xx} and the transverse resistivity (also called Hall resistivity) ρ_{xy} are separated using the following equations:

$$\rho_{xx} = \frac{\rho_{\text{meas}}(+B) + \rho_{\text{meas}}(-B)}{2}, \quad \rho_{xy} = \frac{\rho_{\text{meas}}(+B) - \rho_{\text{meas}}(-B)}{2} \times \frac{L}{W}. \quad (\text{S8})$$

Figure S5a displays the measured resistivity at 0T, 9T and -9T. The disagreement between the 9T and -9T data is evidence of the mutual presence of the longitudinal and transverse resistivities ρ_{xx} and ρ_{xy} . After separating ρ_{xx} and ρ_{xy} using Eq. (S8), as shown in Figure S5b and c, we then calculated zT according to:

$$zT = \frac{S_{xx}^2 T}{\rho_{xx} \kappa_{xx}}. \quad (\text{S9})$$

From the plot of zT in Figure S5d, we note that, although the power factor (shown in Figure 2f in the main text) is record-breaking in magnitude, the zT does not attain a very high value due to the significant thermal conductivity.

It should be noted that the giant magnetic field-induced Seebeck coefficients cannot be observed in the case of $B \parallel a \parallel j_Q$, which is evidenced by comparison of two geometries in Figure S5e and f. This indicates that the giant magnetic field-induced longitudinal and transverse Seebeck coefficients in the case of $B \parallel c \perp j_Q$ originate from the quantized protection of the thermoelectric Hall Effect.

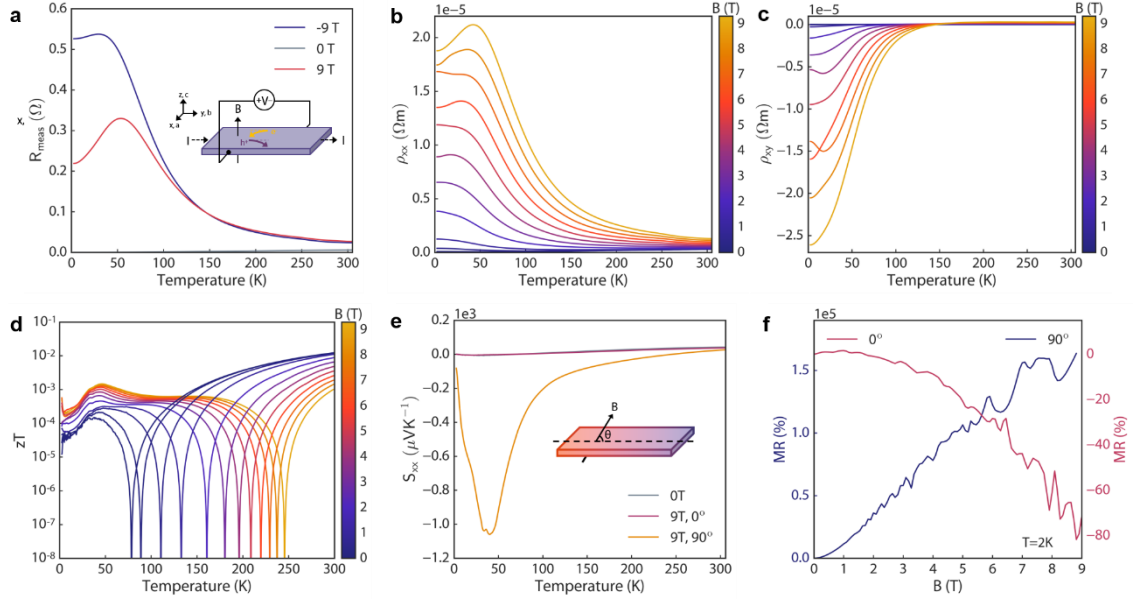


Figure S5. (a) Measured resistivities of TaP at 0T, 9T and -9T for the diagonal offset probe geometry. Inset: Schematic diagram of the electrical transport measurement. Longitudinal and transverse resistivities (c) ρ_{xx} , (d) ρ_{xy} as functions of temperature at different magnetic fields. Comparison of the $B||a||j_Q$ and $B||c||j_Q$ geometries for (f) S_{xx} and (g) MR . The giant Seebeck coefficients were not observed in the $B||a||j_Q$ case.

VI. Thermoelectric Hall Conductivity

To validate the quantized thermoelectric Hall effect, particularly the quantized plateau of the thermoelectric Hall coefficient α_{xy} in the high magnetic field limit, we calculated α_{xy} using the following equation:

$$\alpha_{xy} = \frac{\rho_{xy}S_{xx} + \rho_{xx}S_{xy}}{\rho_{xx}^2 + \rho_{xy}^2}. \quad (\text{S10})$$

To obtain α_{xy} as a function of magnetic field for different temperatures, we replotted S_{xx} and S_{xy} from Figure S4e and f, and ρ_{xx} and ρ_{xy} from Figure S5b and c, as functions of magnetic field, as shown in Figures 2d and 3a in the main text and S6a and b here. The resulting α_{xy} calculated with Eq. (S10) is displayed in Figure 3b in the main text.

To extract the values of effective Fermi velocity v_F^{eff} and chemical potential μ , as well as identify the quantized value of α_{xy}/T approached at very large fields, we fit our low-temperature α_{xy} data up to $T=10\text{K}$ using the general expression of α_{xy} in the dissipationless limit^{S2} (Eq. (3) of the main text):

$$\alpha_{xy} = \frac{eN_f}{2\pi\hbar} \sum_{n=0}^{\infty} \int_0^{\infty} \frac{dk_z}{\pi} \left[s\left(\frac{\varepsilon_n^0(k_z) - \mu}{k_B T}\right) + s\left(\frac{\varepsilon_n^0(k_z) + \mu}{k_B T}\right) \right]. \quad (\text{S11})$$

where N_f equals the number of Weyl points, and $\varepsilon_n^0(k_z)$ denote the Landau level energies:

$$\varepsilon_n^0(k_z) = \text{sgn}(n)v_F\sqrt{2e\hbar B|n| + \hbar^2 k_z^2}. \quad (\text{S12})$$

and v_F is treated as v_F^{eff} . The function $s(x)$ is the entropy per carrier, given by

$$s(x) = -k_B \left[n_F(x) \ln n_F(x) + (1 - n_F(x)) \ln (1 - n_F(x)) \right]. \quad (\text{S13})$$

where $n_F(x) = \frac{1}{1 + e^{\beta x}}$ is the Fermi-Dirac distribution. The fit using Eq. (S11) is shown in Figure S6c, and we extrapolate the fitted function to even larger magnetic fields, revealing we are near the onset of the quantized limit, shown in the inset. The value of α_{xy}/T approached in this limit is $\sim 0.6 \text{ AK}^{-2}\text{m}^{-1}$. The corresponding fitted parameters are given in Figure S6d and e, and in Figure 3e of the main text.

To verify this fit, we additionally fit our low-temperature data using the expression for α_{xy}/T which also includes a finite scattering time τ and is thus a more expressive form for data with weak scattering present^{S2}:

$$\alpha_{xy} = \frac{N_f}{18} \frac{e^2 k_B^2 T v_F \tau^2 B}{\hbar^3} \frac{1 + 3\omega_c^2(E_F)\tau^2}{(1 + \omega_c^2(E_F)\tau^2)^2}. \quad (\text{S14})$$

where the cyclotron frequency ω_c is given by

$$\omega_c(\varepsilon) = \frac{eBv_F^2}{\varepsilon}. \quad (\text{S15})$$

and once again v_F is treated as v_F^{eff} . This fit is shown in Figure S6f with the corresponding fitted parameters shown in Figure S6g and h, which are in good agreement with those of the previous fit.

Similarly, we fit our high-temperature data in the limit of weak scattering using

$$\alpha_{xy} = \frac{N_f e^2 k_B^2 T v_F \tau^2 B}{6\pi^2 \hbar^3} \int_{-\infty}^{+\infty} dx \frac{x^4 e^x}{(1 + e^x)^2} \frac{1}{x^2 + \omega_c^2(k_B T) \tau^2}. \quad (\text{S16})$$

which is shown in Figure S6i with corresponding fitted parameters in S6j and k.

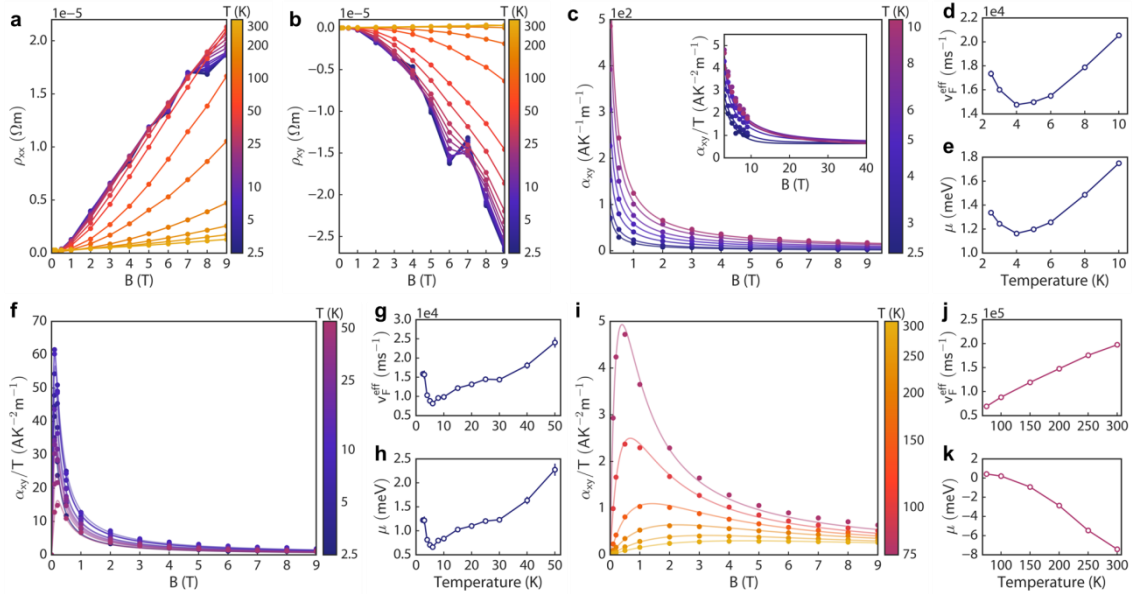


Figure S6. Longitudinal and transverse resistivities (a) ρ_{xx} and (b) ρ_{xy} as functions of magnetic field at different temperatures. (c) Thermoelectric Hall coefficient α_{xy} as a

function of magnetic field at different temperatures. Fitted curves of Eqn. S11 (low-temperature dissipationless limit) are shown as solid lines. (d-e) Effective Fermi velocity and chemical potential parameters obtained from the fit in (c). (d) Fitting with Eqn. S14 and corresponding fitted parameters (e-f). (i) Fitting with Eqn. S16 (high-temperature limit with weak scattering) and corresponding fitted parameters (j-k).

VII. Consistency of Charge Neutrality

Our results from different measurements show a high level of consistency with one another. Taking charge neutrality as an example, we observe excellent agreement between the temperatures of the charge neutral point in the carrier concentration data and in the Seebeck coefficient data. In the plot of the carrier concentrations of electrons and holes as functions of temperature (the top panel of Figure S7) the electron and hole concentrations become equal at around 100K while the Seebeck coefficient at 0T changes its sign at around 75K, as shown in the bottom panel of Figure S7.

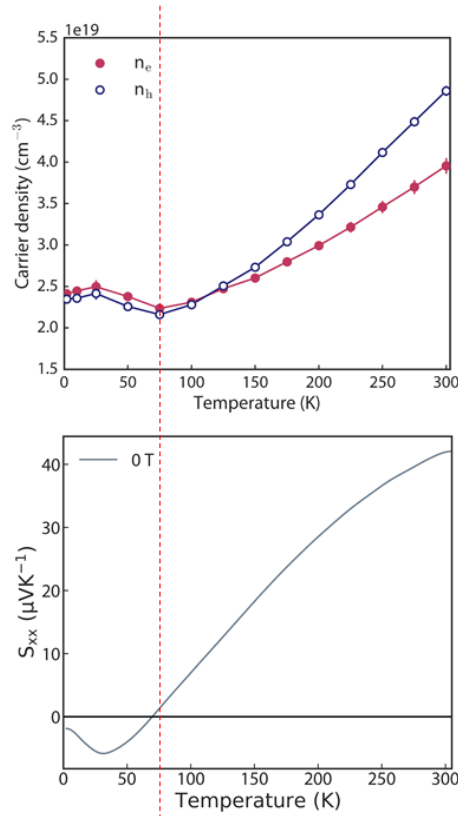


Figure S7. Consistency of the charge neutral point in carrier concentration and Seebeck coefficient.

VIII. X-Ray and Neutron Scattering Measurement Details

Measurements of the phonon modes along high-symmetry lines in the Brillouin zone of TaP were performed using both inelastic x-ray scattering and inelastic neutron scattering. Selected raw intensity spectra along high symmetry direction Γ to Σ are shown in Figure S8 using x-rays (left) and neutrons (right). The spectra were analyzed by a damped harmonic oscillator (DHO) model convoluted with the experimental resolution function to yield the energy and intensity of each mode. These were used to generate a phonon dispersion relation, which can be seen in Figure 4c in the main text, along high symmetry line Z - Γ - Σ . These experimental results serve as a consistency check to support the *ab initio* calculations performed for the thermal conductivity used in the main text and displayed in Figure 4b.

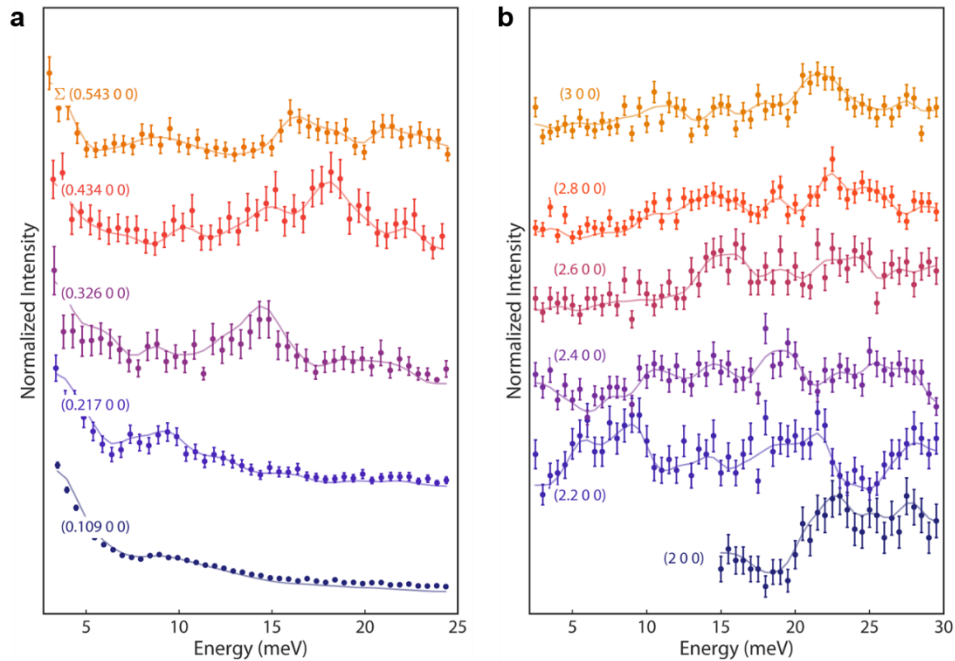


Figure S8. X-ray (left panel) and neutron (right panel) inelastic scattering measurements along the high symmetry direction Γ - Σ . The faint solid lines are a guide for the eye.

IX. Separation of Phonon and Electron Contributions to Thermal Conductivity

To check the compliance or violation of the Wiedemann-Franz law, the phononic and electronic contributions to thermal conductivity need to be separated.

To separate the phononic and electronic contributions, we fit κ_{xx} versus B curves with the following empirical equation:

$$\kappa_{xx}(T, B) = \kappa_{xx}^{ph}(T) + \frac{\kappa_{xx}^e(T, B=0T)}{1 + \beta_e(T)B^m}. \quad (S17)$$

where $\beta_e(T)$ is proportional to the zero-field electronic mean free path of electrons, and m is related to the nature of the electron scattering^{S4, S5, S6}.

Figures S9b-d shows the gradual suppression of κ_{xx} at high magnetic fields at typical temperatures 100K, 200K and 300K. We can see at 100K, κ_{xx} forms a plateau above 4T, indicating that the electronic thermal conductivity is almost completely suppressed, while at 200K and 300K, the suppression is still in an intermediate state. All the κ_{xx} versus B curves can be fitted well with Eq. (S17) and the fitting process for different temperatures successfully achieves the separation of the phononic and electronic contributions to thermal conductivity. The resulting phononic and electronic thermal conductivities are discussed in detail in the main text. Here we stress that the fitting parameter $\beta_e(T)$ obtained from the fitting shows a typical behavior of thermally elevated electron-phonon scattering, as shown in Figure S9a, and the fitting parameter n

fluctuates around 1.35, indicating its constant nature which implies that our fitting process is reasonable.

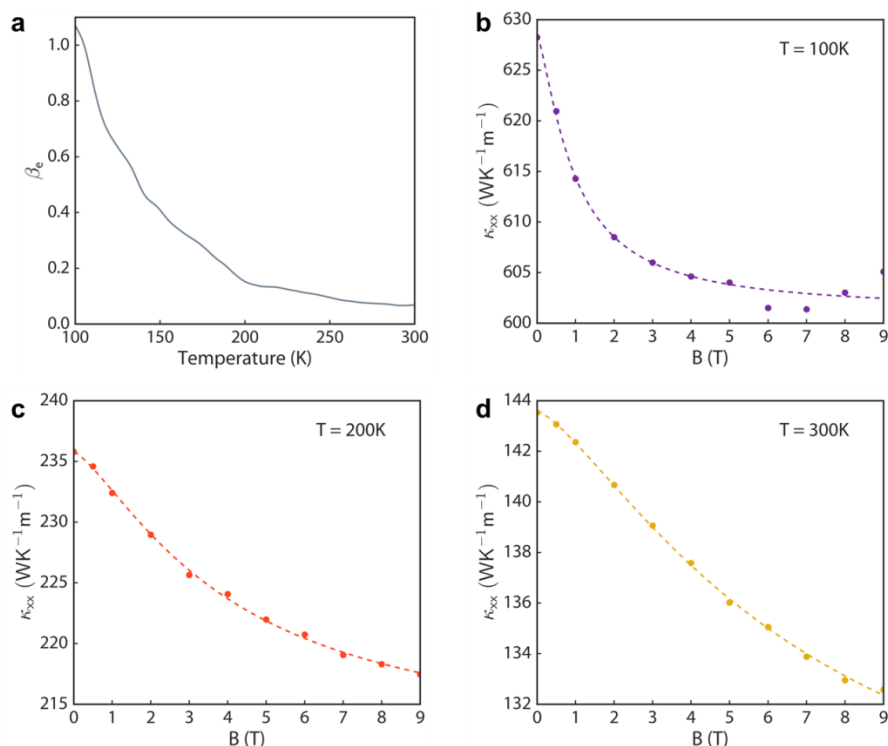


Figure S9. (a) The fitting parameter $\beta_e(T)$ as a function of temperature. The fitting for the κ_{xx} versus B curves at (b) 100K, (c) 200K and (d) 300K.

References

- S1. Skinner, B. & Fu, L. Large, nonsaturating thermopower in a quantizing magnetic field. *Science Advances* **4**, eaat2621, doi: 10.1126/sciadv.aat2621 (2018).
- S2. Kozii, V., Skinner, B. & Fu, L. Thermoelectric Hall conductivity and figure of merit in Dirac/Weyl materials. *eprint arXiv:1902.10123*, arXiv:1902.10123 (2019).
- S3. Murakawa, H. et al. Detection of Berry's Phase in a Bulk Rashba Semiconductor. *Science* **342**, 1490, doi:10.1126/science.1242247 (2013).

- S4. Ocana, R. *et al.* Thermal conductivity tensor in $\text{YBa}_2\text{Cu}_3\text{O}_{7-x}$: Effects of a planar magnetic field. *Phys. Rev. B* **66**, 064525, doi: 10.1103/PhysRevB.66.064525 (2002).
- S5. Pogorelov, Y. *et al.* Mechanisms of heat conductivity in high- T_c superconductors. *Phys. Rev. B* **51**, 15474, doi: 10.1103/PhysRevB.51.15474 (1995).
- S6. Yu, F. *et al.* Tensor Magnetothermal Resistance in $\text{YBa}_2\text{Cu}_3\text{O}_{7-x}$ via Andreev Scattering of Quasiparticles. *Phys. Rev. Lett.* **74**, 5136, doi: 10.1103/PhysRevLett.74.5136 (1995).